

SPA-VAE: Similar-Parts-Assignment for Unsupervised 3D Point Cloud Generation

Shidi Li¹, Christian Walder^{1,2*}, Miaomiao Liu¹

¹Australian National University

²Data61, CSIRO

{shidi.li, christian.walder, miaomiao.liu}@anu.edu.au,

Abstract

This paper addresses the problem of unsupervised parts-aware point cloud generation with learned parts-based self-similarity. Our SPA-VAE infers a set of latent canonical candidate shapes for any given object, along with a set of rigid body transformations for each such candidate shape to one or more locations within the assembled object. In this way, noisy samples on the surface of, say, each leg of a table, are effectively combined to estimate a single leg prototype. When parts-based self-similarity exists in the raw data, sharing data among parts in this way confers numerous advantages: modeling accuracy, appropriately self-similar generative outputs, precise in-filling of occlusions, and model parsimony. SPA-VAE is trained end-to-end using a variational Bayesian approach which uses the Gumbel-softmax trick for shared part assignments, along with various novel losses to provide appropriate inductive biases. Quantitative and qualitative analyses on ShapeNet demonstrate the advantage of SPA-VAE.

1 Introduction

Significant progress has been made recently in unsupervised 3D shape segmentation by using primitives (Tulsiani et al. 2017; Paschalidou, Ulusoy, and Geiger 2019; Sun et al. 2019; Yang and Chen 2021; Paschalidou, Gool, and Geiger 2020) and implicit representations (Chen et al. 2019; Deng et al. 2020; Genova et al. 2019, 2020; Paschalidou et al. 2021; Li et al. 2021), which has further boosted parts-based controllable generation (Shu, Park, and Kwon 2019) and editing (Li, Liu, and Walder 2022; Li et al. 2021; Yang et al. 2021; Gal et al. 2021). For example, recently Li, Liu, and Walder (2022) achieved unsupervised parts-based controllable generation and editing by learning a disentangled (pose and shape) and dual (primitive and points) representation for 3D shapes. However, existing parts-aware segmentation and generation approaches (Paschalidou, Gool, and Geiger 2020; Li, Liu, and Walder 2022) focus on parsing or modelling the object’s parts in spatial locations dependent on the category of the object. Due to the potentially imbalanced distribution of points across different parts of an object, existing methods suffer from inferior generation and segmentation results for parts with a small number of points, even when those parts are duplicated throughout the object, meaning that greater detail may be inferred.

*Now at Google Brain Montreal.

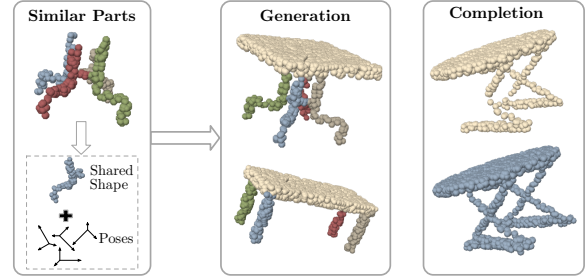


Figure 1: SPA-VAE learns self-similarity by disentangling parts of the (unlabeled) input point cloud that have the same shape but different poses, allowing parts-aware generation and completion. With parts denoted by different colors, here we demonstrate: parts-aware *generation* with similar table legs, and *completion* (blue) via the inferred self-similarity of the incomplete input (yellow).

To address this problem, we propose to learn parts-based self-similarity in an unsupervised manner, to infer a set (per object instance) of canonical shapes for point cloud generation. In particular, we model the similarity between parts by letting them share a *canonical shape* instantiated with multiple poses. This is more general than a symmetry based notion of self-similarity wherein one part may be corresponded to another by mirroring across a particular hyper-plane. Rather, our notion of parts-based self-similarity needs only correspond (by rigid body transformation) one or more observed noisy or occluded parts to their object-instance-specific *canonical shape*.

In this paper, we propose SPA-VAE, an unsupervised VAE-based framework for point cloud generation which infers and exploits parts-based self-similarity. We seek to discover the *canonical shapes* underlying an object, to disentangle the observed parts’ poses defined by rigid transformations relative to a canonical shape coordinate system, and to model the associated joint distribution for generation. Our model disentangles poses, primitives, and points similarly to Li, Liu, and Walder (2022), by leveraging a specially designed disentanglement-oriented VAE framework (Higgins et al. 2016; Burgess et al. 2018). This yields part information at specific spatial locations. We further propose the Similar Parts Assignment (SPA) module as a mechanism for infer-

ring a set of *canonical shapes* for an object, along with an assignment matrix which associates each *canonical shape* with one or more poses, allowing to assemble the object. To handle the non-differentiability of this hard assignment matrix, we apply the *straight-through Gumbel-softmax* gradient approximation (Jang, Gu, and Poole 2016; Maddison, Mnih, and Teh 2016), which has been widely used in 3D computer vision (Yang et al. 2019b). We further introduce a *diversity loss* to encourage our network to learn discriminative *canonical shapes*, and an *assignment loss* to guarantee the existence of *canonical shapes*. In addition to the quantitatively improved shape generation due to parts-based self-similarity learning, SPA-VAE further yields intelligent shape completion at no extra cost.

In summary, our main contributions are as follows:

1. We propose a framework for modelling parts-based self-similarity for 3D shape modelling and generation.
2. We provide a practical scheme based on the Gumbel-softmax trick for the non-differentiable parts assignment matrix, along with novel loss terms which we demonstrate to provide effective inductive biases.
3. We demonstrate that our disentangled canonical shapes, assignment matrix and part poses improve point cloud generation and allow shape completion.

Extensive qualitative and quantitative results on the popular SHAPENET data set demonstrate the excellent performance that is obtainable by the novel similar-parts-assignment mechanism exemplified by our SPA-VAE model.

2 Related Work

Parts-Aware 3D Point Cloud Generation. The topic of 3D point cloud generation has been widely studied in recent years (Achlioptas et al. 2018; Valsesia, Fracastoro, and Magli 2018; Hui et al. 2020; Wen, Yu, and Tao 2021; Kim et al. 2020; Klokov, Boyer, and Verbeek 2020), especially by learning deformation from vanilla point clouds or shapes (Yang et al. 2019a; Cai et al. 2020; Luo and Hu 2021; Zhou, Du, and Wu 2021; Li et al. 2021). Another branch of work focuses on parts-aware point cloud generation with ground-truth semantic labels (indicating whether any given point belongs to *e.g.* the base, back, or legs of a chair) (Nash and Williams 2017; Mo et al. 2019, 2020; Schor et al. 2019; Yang et al. 2021). As the requirement for well-aligned semantic part labels hinders real-world application, unsupervised parts-aware generation has been explored by Li, Liu, and Walder (2022); Shu, Park, and Kwon (2019); Li et al. (2021); Postels et al. (2021); Gal et al. (2021). In particular, Li et al. (2021) generates parts point clouds by utilizing the space consistent feature of the sphere, while Shu, Park, and Kwon (2019) organizes points by way of a latent tree structure, and Li, Liu, and Walder (2022) further disentangled parts into their pose and shape, to achieve the controllable editing. Finally, dozens of 3D shape reconstruction algorithms may potentially be applied to 3D point cloud generation (Chen et al. 2019; Paschalidou et al. 2021; Paschalidou, Gool, and Geiger 2020; Dubrovina et al. 2019). However, the above works ignore parts-based self-similarity, which may benefit fitting and generation by effectively sharing data

for each part with the similar counterparts within the object (as in *e.g.* the legs of a table).

Unsupervised Self-Similarity Learning. Exploiting the self-symmetry or similarity property (Huang and You 2012) has broad applications in image retrieval (Yoon et al. 2020; Diao et al. 2021; Mishra et al. 2021; Xiao et al. 2021; Seo, Shim, and Cho 2021; Wu, Rupprecht, and Vedaldi 2020), video-based action recognition (Kwon et al. 2021), music modelling (Walder and Kim 2018b) and depth map estimation (Xu et al. 2020; Zhou, Liu, and Ma 2021). In particular, Zhou, Liu, and Ma (2021) detects planes of symmetry within input images in an unsupervised manner by building a 3D cost volume. While detecting the symmetric structure can improve the object geometry, such as the depth estimation, it is challenging to directly extend such approaches to parts-aware object segmentation and generation due to the complexity of modeling mutual symmetries within groups of parts. Our SPA-VAE explores the self-similarity instead of self-symmetry for unsupervised learning of canonical shapes and object pose distributions, and contributes similar-parts-aware generation.

3D Point Cloud Completion. The symmetry property has been explored in the 3D shape completion task in the literature (Mitra, Guibas, and Pauly 2006; Mitra et al. 2013; Pauly et al. 2008; Podolak et al. 2006; Sipiran, Gregor, and Schreck 2014; Sung et al. 2015; Thrun and Wegbreit 2005). Traditional geometry-based approaches require expensive optimizations and are sensitive to noise. Recent learning-based methods achieve superior performance especially in a supervised setting with paired complete shapes (Xiang et al. 2021; Xie et al. 2021; Gong et al. 2021; Wang, Ang, and Lee 2021; Wen et al. 2021b; Huang et al. 2021; Nie et al. 2020; Xie et al. 2020; Wang, Ang Jr, and Lee 2020a; Yuan et al. 2018; Tchapmi et al. 2019). The lack of pairs of complete and incomplete data in real world settings, however, hinders the general applicability. Recently, methods not based on such pairings have been proposed for the shape completion task (Wang, Ang Jr, and Lee 2020b; Gu et al. 2020; Wen et al. 2021a; Chen, Chen, and Mitra 2019; Stutz and Geiger 2018; Wu et al. 2020; Zhang et al. 2021). In particular, Chen, Chen, and Mitra (2019) maps reconstructed incomplete inputs to a latent space to imitate the complete one using GANs (Goodfellow et al. 2014), while the subsequent (Zhang et al. 2021) adopts GAN inversion (Karras, Laine, and Aila 2019; Brock, Donahue, and Simonyan 2018) to find a best match from incomplete point clouds to reconstructed complete ones. In comparison with existing methods, our model (which does not require pairs of incomplete and complete point clouds) merely leverages complete point clouds in training and incomplete ones in testing, by leveraging our inferred parts-based self-similarities in an unsupervised manner.

3 Methodology

The focus of our SPA-VAE is on learning parts-based self-similarity for parts-aware 3D shape generation and completion — see Fig. 2 for an architectural overview, and Appendix A of the supplementary material for an overview

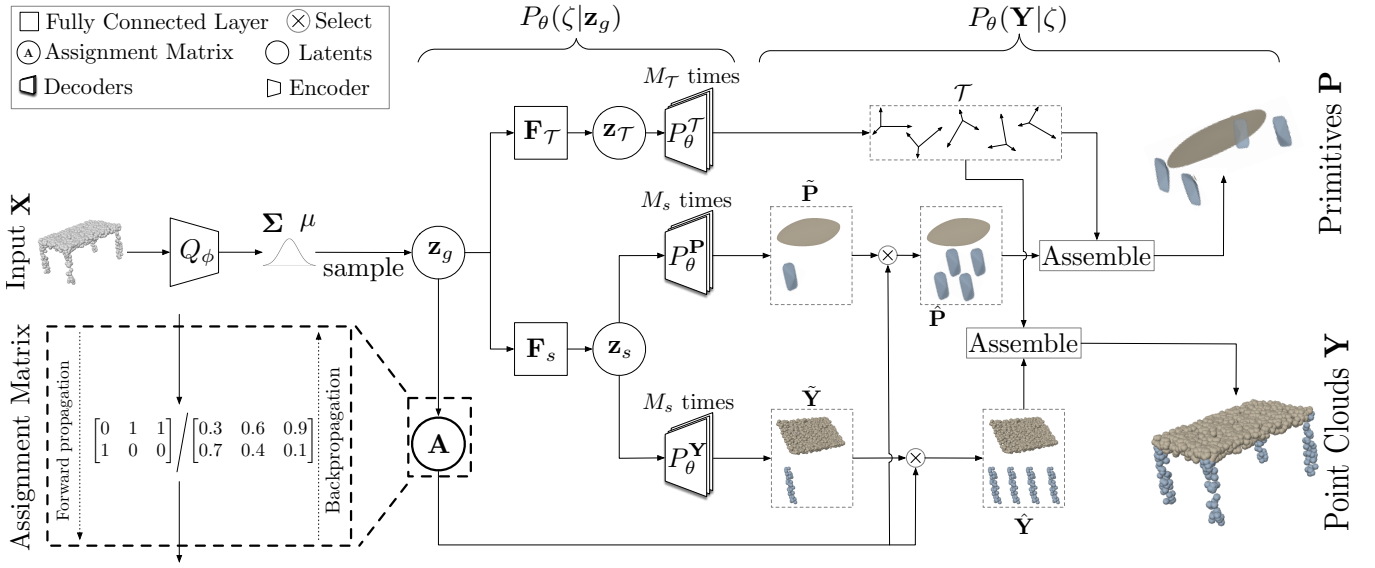


Figure 2: An overview of the SPA-VAE architecture. Simplified from (Li, Liu, and Walder 2022), the encoder Q_ϕ first infers the posterior from the input ground-truth point cloud $\mathbf{X} \in \mathbf{R}^{N \times 3}$. The global latent \mathbf{z}_g is then sampled from the posterior using the reparameterization trick, from which the shared shape latent \mathbf{z}_s and pose latent \mathbf{z}_τ are obtained from fully connected layers F_s and F_τ , respectively. Further, poses and shapes (primitives and points) are reconstructed from the corresponding latents by pose decoders P_θ^T , primitive decoders P_θ^P , and point decoders P_θ^Y , respectively. In another branch, the assignment matrix \mathbf{A} is calculated as a function of the global latent \mathbf{z}_g , and represents parts similarity by denoting the sharing of shapes across multiple poses. Assigned poses and shapes are finally assembled to yield the reconstructed set of primitives \mathbf{P} and point cloud \mathbf{Y} .

of our notation. To learn the notion of self-similarity introduced in Sec. 1, SPA-VAE disentangles 3D point clouds into the constituent pose and shape information of the parts therein, employing a disentanglement-oriented form of the Variational Auto-Encoder (VAE) framework (Burgess et al. 2018; Higgins et al. 2016). Similar to Li, Liu, and Walder (2022), our resulting VAE-based model may be defined via an *Evidence lower bound* (ELBO) objective (Kingma and Welling 2013; Rezende, Mohamed, and Wierstra 2014) as

$$\log P_\theta(\mathbf{X}) \geq \quad (1)$$

$$E_{Q_\phi(\mathbf{z}_g|\mathbf{X})}[\log P_\theta(\mathbf{X}|\zeta)] - D_{KL}(Q_\phi(\mathbf{z}_g|\mathbf{X})\|P_\theta(\mathbf{z}_g)).$$

The first r.h.s. term is the *reconstruction error* and the second the *variational regularizer*, while Q_ϕ and P_θ are the encoder and decoder, respectively. Here ζ denotes our *disentangled* representation (defined shortly), and we approximate the posterior in ζ by learning an approximate posterior $Q_\phi(\mathbf{z}_g|\mathbf{X})$ of a latent *global* (non-disentangled) representation \mathbf{z}_g via the ELBO. Following (Li, Liu, and Walder 2022) we couple ζ and \mathbf{z}_g by way of a learnt deterministic mapping, *i.e.* by choosing $P_\theta(\zeta|\mathbf{z}_g) = Q_\phi(\zeta|\mathbf{z}_g) \rightarrow \delta(\zeta - \text{NN}_\theta(\mathbf{z}_g))$, with $\delta(\cdot)$ as Dirac distribution and NN_θ be a neural network model. As a result, we may define $\zeta = \text{NN}_\theta(\mathbf{z}_g)$, which denotes the 3D shape corresponding to the global latent \mathbf{z}_g . The 3D shape is further decomposed into M_τ constituent parts as $\zeta = \bigcup_{m=1}^{M_\tau} \zeta^m$. Each part is also decomposed further, as

$$\zeta^m = \{\mathcal{T}^m, \hat{\mathbf{Y}}^m, \hat{\mathbf{P}}^m\}, \quad (2)$$

which represents the pose \mathcal{T}^m , primitive $\hat{\mathbf{P}}^m$, and points $\hat{\mathbf{Y}}^m$. We also — particularly in Fig. 2 — use the notation $\hat{\mathbf{Y}} = \bigcup_{m=1}^{M_\tau} \hat{\mathbf{Y}}^m$, *etc.* The three components which make up a single part are defined as follows.

Pose \mathcal{T}^m includes translation $\mathbf{t} \in \mathbf{R}^3$ and rotation $\mathbf{R}(\mathbf{q}) \in \text{SO}(3)$. Rotation is further defined by the quaternion $\mathbf{q} \in \mathbf{R}^3$; for details see (Li, Liu, and Walder 2022). These parameters represent the *linear* transformation of a single part from canonical pose to object pose as $\mathbf{x} \mapsto \mathcal{T}(\mathbf{x}) \equiv \mathbf{R}(\mathbf{q})\mathbf{x} + \mathbf{t}$.

Primitive $\hat{\mathbf{P}}^m$ is deformed *linearly* and *non-linearly* from simple shapes. We employ the superquadric parametrization with parameters η and ω as in (Paschalidou, Ulusoy, and Geiger 2019; Li, Liu, and Walder 2022). Thus, the surface point is defined (in canonical coordinates) by:

$$\mathbf{r}(\eta, \omega) = \begin{bmatrix} \alpha_x \cos^{\epsilon_1} \eta \cos^{\epsilon_2} \omega \\ \alpha_y \cos^{\epsilon_1} \eta \sin^{\epsilon_2} \omega \\ \alpha_z \sin^{\epsilon_1} \eta \end{bmatrix} \begin{matrix} -\pi/2 \leq \eta \leq \pi/2 \\ -\pi \leq \omega \leq \pi \end{matrix}, \quad (3)$$

where $\boldsymbol{\alpha} = (\alpha_x, \alpha_y, \alpha_z)^\top$ and $\boldsymbol{\epsilon} = (\epsilon_1, \epsilon_2)^\top$ are the scale and shape parameters, respectively. We further include two *non-linear* deformation parameters as in (Li, Liu, and Walder 2022; Barr 1987; Paschalidou, Ulusoy, and Geiger 2019).

Points $\hat{\mathbf{Y}}^m$ are 3D point clouds representing a single part in canonical coordinates with dimensionality $\mathbf{R}^{N_p \times 3}$, so that N_p is number of points per part.

3.1 Similar Parts Assignment (SPA)

To achieve self-similarity within the assembled object, we share each of a set of M_s *shapes* (each comprising a primitive and point cloud) across $M_{\mathcal{T}} \geq M_s$ *parts* (each with unique pose). Shapes are not fixed across objects, but rather are latent variables which form part of the generation process for a given object. This is achieved by modelling

- a set of M_s latent *shapes* defined by their primitives $\tilde{\mathbf{P}} = \bigcup_{m=1}^{M_s} \tilde{\mathbf{P}}^m$ along with the corresponding point clouds $\tilde{\mathbf{Y}} = \bigcup_{m=1}^{M_s} \tilde{\mathbf{Y}}^m$,
- an assignment matrix $\mathbf{A} \in \{0, 1\}^{M_s \times M_{\mathcal{T}}}$ which associates each of the $M_{\mathcal{T}}$ latent part transformations $\mathcal{T}^1, \dots, \mathcal{T}^{M_{\mathcal{T}}}$ with exactly one of M_s latent shapes.

The j -th column \mathbf{A}_j of \mathbf{A} is a one-hot vector which indicates which shape is coupled with the j -th pose. Precisely, this means that if $A_{ij} = 1$, then

$$\tilde{\mathbf{P}}^i = \hat{\mathbf{P}}^j \quad \text{and} \quad \tilde{\mathbf{Y}}^i = \hat{\mathbf{Y}}^j, \quad (4)$$

where we emphasize that *e.g.* $\tilde{\mathbf{P}}^i$ represents the i -th latent shape primitive, while $\hat{\mathbf{P}}^j$ denotes the j -th primitive appearing in the object as per Eq. 2 (and therefore coupled with the j -th pose \mathcal{T}^j) — see the notation guide in Appendix A.

To handle the categorical assignment matrix \mathbf{A} we employ the *Gumbel-softmax trick* and associated *straight-through* gradient estimator (Maddison, Mnih, and Teh 2016; Jang, Gu, and Poole 2016). This means that \mathbf{A}_j is defined as, for $j = 1, 2, \dots, M_{\mathcal{T}}$,

$$\mathbf{A}_j = \text{one.hot}(\arg \max_i \Delta_{\theta}(\mathbf{z}_g)_j), \quad (5)$$

where $\Delta_{\theta}(\cdot)$ is a neural network module which maps the global latent \mathbf{z}_g to a matrix of dimensionality $\mathbf{R}^{M_s \times M_{\mathcal{T}}}$, while $\text{one.hot}(\cdot)$ maps the index returned by the $\arg \max$ function to $\{0, 1\}$ indicator form.

Because \mathbf{A} is not differentiable w.r.t θ , we employ the straight-through estimator on the soft assignment

$$\tilde{\mathbf{A}}_j = \sigma \left(\frac{\log(\Delta_{\theta}(\mathbf{z}_g)_j) + \mathbf{g}_j}{\tau} \right), \quad (6)$$

for some fixed $\tau > 0$ where each $\mathbf{g}_j \in \mathbf{R}^{M_s}$ is sampled i.i.d. from the Gumbel distribution so that $\mathbf{g}_{ij} = -\log(-\log u_{ij})$ where $u_{ij} \sim \text{Uniform}(0, 1)$. The sigmoid function is defined as usual as

$$\sigma(v)_i = \frac{\exp(v_i)}{\sum_{j=1}^{M_s} \exp(v_j)}. \quad (7)$$

Since the assignment of shapes to parts is *hard*, the softmax formulation is not applicable in our case; *e.g.*, we cannot have 90% of one shape and 10% of another. We resolve this by using Eq. 5 in forward propagation with the gradient of Eq. 6 in back propagation, the well-known straight-through Gumbel-softmax estimator (Jang, Gu, and Poole 2016).

3.2 Object Generation by Assembling Parts

We now cover how the latent poses, primitives, points, and assignment matrix may be generated and assembled into an object (*e.g.* comprising a point cloud \mathbf{Y} and set of parts ζ in non-canonical coordinates). M_s primitives (together denoted $\tilde{\mathbf{P}}$) are sampled by sampling each of the associated η and ω parameters. The assignment matrix \mathbf{A} is also sampled along with the poses \mathcal{T} . The canonical object part primitives $\hat{\mathbf{P}}$ are then selected with replacement from the canonical candidate shape primitives $\tilde{\mathbf{P}}$ via the assignment matrix and transformed by the pose transformations (see (Li, Liu, and Walder 2022) for transforming a superquadric) to obtain the object primitives in object coordinates, \mathbf{P} (see Fig. 2 and the notation guide in Appendix A of the supplementary).

Similarly, M_s canonical point clouds are generated by point-decoder neural network modules, and combined via the assignment matrix and part poses to yield $N = N_p \times M_{\mathcal{T}}$ number of 3D points in the generated point cloud, which we denote by \mathbf{Y} (see Fig. 2).

The above steps are shared in both reconstruction and generation, except that the global latent \mathbf{z}_g is encoded from the input ground-truth point cloud \mathbf{X} in reconstruction and training, whereas it is sampled from the standard Gaussian prior in (unconstrained) generation.

3.3 Losses

We now cover the terms in the reconstruction error of Eq. 1. These are designed to provide an effective inductive bias for unsupervised part segmentation, primitive representation, point reconstruction, and self similarity.

Points distance $\mathcal{L}_p(\mathbf{X}, \mathbf{Y})$ is defined by the mean of parts Chamfer distance as in Li, Liu, and Walder (2022),

$$\mathcal{L}_p(\mathbf{X}, \mathbf{Y}) = \sum_{m=1}^{M_{\mathcal{T}}} \mathcal{L}_c(\hat{\mathbf{X}}^m, \hat{\mathbf{Y}}^m), \quad (8)$$

where $\mathcal{L}_c(\cdot)$ denotes Chamfer distance (Li, Liu, and Walder 2022), \mathbf{X}^m is subset of the input point cloud \mathbf{X} with nearest primitive \mathbf{P}^m , and $\hat{\mathbf{X}}^m = (\mathcal{T}^m)^{-1}(\mathbf{X}^m)$ is the same mapped to the canonical coordinate system. In addition, $\hat{\mathbf{Y}}^m \in \mathbf{R}^{N_p \times 3}$ is the point cloud output selected by the one-hot vector \mathbf{A}_m from M_s points decoders outputs, as in Sec. 3.1.

Primitives to points distance $\mathcal{L}_r(\mathbf{X}, \mathbf{P})$ measures the distance between primitive \mathbf{P} and point cloud \mathbf{X} ,

$$\mathcal{L}_r(\mathbf{X}, \mathbf{P}) = \mathcal{L}_{\mathbf{P} \rightarrow \mathbf{X}}(\mathbf{X}, \mathbf{P}) + \mathcal{L}_{\mathbf{X} \rightarrow \mathbf{P}}(\mathbf{X}, \mathbf{P}), \quad (9)$$

where $\mathcal{L}_{\mathbf{P} \rightarrow \mathbf{X}}$ denotes the directed distance from primitives to points, and *vice versa*. We follow (Li, Liu, and Walder 2022; Paschalidou, Ulusoy, and Geiger 2019) but with $\mathcal{L}_{\mathbf{X} \rightarrow \mathbf{P}}$ calculated by Eq. 8 rather than Eq. 11 in (Paschalidou, Ulusoy, and Geiger 2019).

Overlapping loss $\mathcal{L}_o(\mathbf{P})$ discourages primitives from overlapping one another, and is formally defined in terms of the smoothed indicator function $H^m(\cdot)$ (Solina and Bajcsy

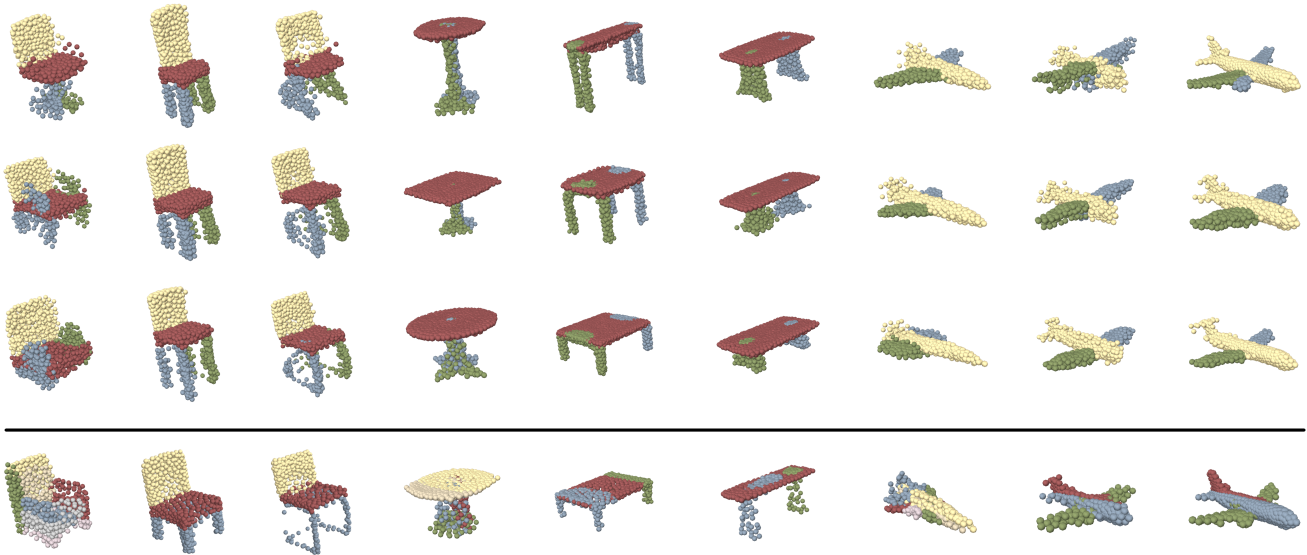


Figure 3: Part-aware generation for the chair, table, and airplane categories. Colored by parts, green and blue parts are mutually similar in all categories, *i.e.* with the same shape but different poses. *Top three rows*: examples generated by SPA-VAE. *Bottom row*: examples generated by EDITVAE from the paper (Li, Liu, and Walder 2022).

1990) as in (Li, Liu, and Walder 2022; Paschalidou, Ulusoy, and Geiger 2019).

$$\mathcal{L}_o(\mathbf{P}) = \frac{1}{M_{\mathcal{T}}} \sum_{m=1}^{M_{\mathcal{T}}} \frac{1}{|\mathcal{S}| - |\mathcal{S}^m|} \sum_{\mathbf{y} \in \mathcal{S} \setminus \mathcal{S}^m} \max(s - H^m(\mathbf{y}), 0), \quad (10)$$

where $|\cdot|$ denotes cardinality, \mathcal{S}^m denotes a set of points sampled from the surface of \mathbf{P}^m , and $\mathcal{S} = \bigcup_{m=1}^{M_{\mathcal{T}}} \mathcal{S}^m$. In addition, s is a threshold parameter associated with $H^m(\cdot)$ to discourage primitives from overlapping, or even avoid it entirely to achieve the spatial disjointness.

Diversity loss $\mathcal{L}_d(\alpha)$ promotes point clouds with highly variable primitive scales. We use a monotonic squashing transformation of what can be shown to be proportional to the sum of the variances of the components of α ,

$$\mathcal{L}_d(\alpha) = \tanh \left(\frac{-c_1 \sum_{i=1}^{M_s} \sum_{j=1, j \neq i}^{M_s} \|\alpha_i - \alpha_j\|_2^2}{M_s(M_s - 1)} \right), \quad (11)$$

where α is from Eq. 3 and we fixed $c_1 = 4$ throughout.

Assignment loss $\mathcal{L}_a(\mathbf{A})$ applies a hinge loss to \mathbf{A} ,

$$\mathcal{L}_a(\mathbf{A}) = \frac{1}{M_s} \sum_{i=1}^{M_s} \max(1 - \sum_{j=1}^{M_{\mathcal{T}}} \mathbf{A}_{ij}, 0), \quad (12)$$

thereby encouraging assignment matrix \mathbf{A} for which each shape is activated at least once.

3.4 Implementation and Training Details

SPA-VAE is trained via the usual ELBO objective Eq. 1, but in a specific stage-wise fashion that enhances training

speed and stability. In stage 1 we train the primitives for 200 epochs, with the reconstruction error in Eq. 1,

$$E_{Q_{\phi}(z_g|\mathbf{X})}[\log P_{\theta}(\mathbf{X}|\zeta)] = \mathcal{L}_r(\mathbf{X}, \mathbf{P}) + \omega_o \mathcal{L}_o(\mathbf{P}) + \omega_d \mathcal{L}_d(\alpha) + \omega_a \mathcal{L}_a(\mathbf{A}). \quad (13)$$

In stage 2 we train primitives and points together with the reconstruction error

$$E_{Q_{\phi}(z_g|\mathbf{X})}[\log P_{\theta}(\mathbf{X}|\zeta)] = \mathcal{L}_p(\mathbf{X}, \mathbf{Y}) + \omega_a \mathcal{L}_a(\mathbf{A}).$$

All encoders decoders match (Li, Liu, and Walder 2022) except the fully connected $\Delta_{\theta}(z_g)$ which generates \mathbf{A} .

4 Experiments

Evaluation metrics, baselines, and details. SPA-VAE is evaluated on the chair, table, and airplane categories of ShapeNet (Chang et al. 2015), with the same data splits and the same evaluation metrics of (Shu, Park, and Kwon 2019; Li, Liu, and Walder 2022), *i.e.* JSD, MMD-CD, MMD-EMD, COV-CD, COV-EMD. We compared our SPA-VAE with four existing models: r-GAN (Achlioptas et al. 2018), Valsesia (Valsesia, Fracastoro, and Magli 2018), TREEGAN (Shu, Park, and Kwon 2019), and EDITVAE (Li, Liu, and Walder 2022). The first of these are baselines which generate point clouds as a whole. In contrast, TREEGAN and EDITVAE achieve parts-aware point cloud generation. Specifically, TREEGAN generates points via a latent tree structure while EDITVAE performs the generation via a disentangled parts-based representation.

All models use input point clouds with 2048 points, and infer (global) latent vector representations $z_g \in \mathbf{R}^{256}$ with standard Gaussian prior. Each generated part consists of 512 points. β -VAE (Burgess et al. 2018; Higgins et al. 2016) is adopted in training to obtain a well disentangled latent.

| Class | Model | JSD ↓ | MMD-CD ↓ | MMD-EMD ↓ | COV-CD ↑ | COV-EMD ↑ |
|----------|--|--------------------|---------------|--------------|-----------|-----------|
| Chair | r-GAN (dense)* | 0.238 | 0.0029 | 0.136 | 33 | 13 |
| | r-GAN (conv)* | 0.517 | 0.0030 | 0.223 | 23 | 4 |
| | Valsesia (no up.)* | 0.119 | 0.0033 | 0.104 | 26 | 20 |
| | Valsesia (up.)* | 0.100 | 0.0029 | 0.097 | 30 | 26 |
| | TREEGAN (Shu, Park, and Kwon 2019) | 0.069 | 0.0018 | 0.113 | 51 | 17 |
| | EDITVAE (Li, Liu, and Walder 2022) ($M = 4$) | 0.047 | 0.0018 | 0.115 | 45 | 29 |
| | SPA-VAE ($M_T = 4$) | 0.065 [†] | 0.0017 | 0.034 | 39 | 23 |
| Airplane | r-GAN(dense)* | 0.182 | 0.0009 | 0.094 | 31 | 9 |
| | r-GAN(conv)* | 0.350 | 0.0008 | 0.101 | 26 | 7 |
| | Valsesia (no up.)* | 0.164 | 0.0010 | 0.102 | 24 | 13 |
| | Valsesia (up.)* | 0.083 | 0.0008 | 0.071 | 31 | 14 |
| | TREEGAN (Shu, Park, and Kwon 2019) | 0.064 | 0.0004 | 0.070 | 45 | 9 |
| | EDITVAE (Li, Liu, and Walder 2022) ($M = 3$) | 0.044 | 0.0005 | 0.067 | 23 | 17 |
| | SPA-VAE ($M_T = 3$) | 0.067 [†] | 0.0004 | 0.003 | 39 | 23 |
| Table | TREEGAN (Shu, Park, and Kwon 2019) | 0.067 | 0.0018 | 0.090 | 45 | 29 |
| | EDITVAE (Li, Liu, and Walder 2022) ($M = 3$) | 0.042 | 0.0017 | 0.130 | 39 | 30 |
| | SPA-VAE ($M_T = 3$) | 0.068 [†] | 0.0016 | 0.020 | 45 | 21 |

Table 1: Generative performance. \uparrow means the higher the better, \downarrow means the lower the better. The score is highlighted in bold if it is the best one compared with state-of-the-art. For network with \star we use the result reported in (Valsesia, Fracastoro, and Magli 2018; Shu, Park, and Kwon 2019; Li, Liu, and Walder 2022). JSD scores marked \dagger can be improved significantly by a simple post-processing as per Tab. 2. Both M_T and M represent the number of object parts.

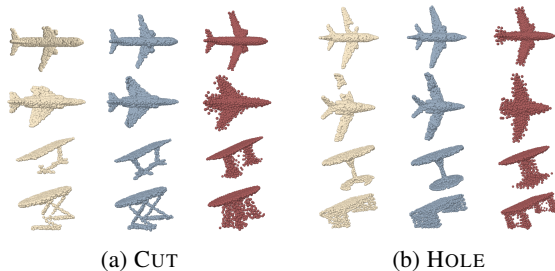


Figure 4: Completion from the a) CUT and b) HOLE corruptions. *Left*: UNCOMPLETED point clouds. *Middle*: completion by COMPLETION-S. *Right*: completion by COMPLETION-R.

We set the dimensionality $z_s \in \mathbf{R}^{32}$ for the shape latent and $z_T \in \mathbf{R}^{16}$ for the pose latent, respectively. We use ADAM (Kingma and Ba 2014) with learning rate 0.0001 for 1000 epochs, a batch size of 30, and no momentum. Code will be provided on publication of the paper.

4.1 Generation

For point cloud generation we sample the global latent z_g , and then compute the corresponding poses, primitives and points along with the assignment matrix — see Fig. 2 for an overview. The components thusly generated are assembled to compose the final point cloud output in the manner described in Sec. 3.2. Quantitative and qualitative results are provided in Tab. 1 and Fig. 3, respectively. Tab. 1 shows that SPA-VAE has competitive numerical performance compared with state-of-the-art approaches. Specifically, SPA-VAE consistently achieves the best performance

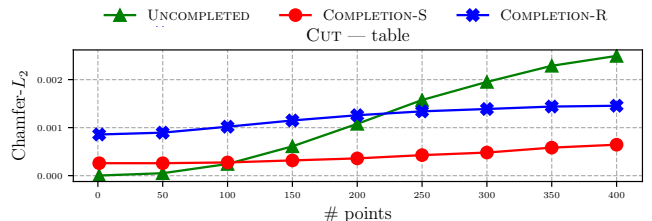


Figure 5: Completion of CUT input point cloud corruptions, for the table category. *Horizontal*: the number of points removed from ground truth point cloud. *Vertical*: the Chamfer distance between the ground truth point cloud and the UNCOMPLETED one (green), or the completed one using either the COMPLETION-R (blue), or COMPLETION-S (red) methods. See Fig. 6 in Appendix D for more categories.

under the MMD-EMD and MMD-CD metrics. In line with our intuition, SPA-VAE performs especially well on the chair and table categories wherein the *i*) the legs are often poorly sampled and *ii*) the style of a chair or table leg is highly variable across object instances, but highly self-similar within them. Note that the number of parts (colored in Fig. 3) equals the number of poses M_T , which is manually selected for each category to achieve a semantically meaningful segmentation with potentially similar parts in our experiments. To the best of our knowledge, EDITVAE is the closest baseline as it also disentangles parts with poses and shapes in an unsupervised manner. But it does not explicitly model parts-based self-similarity. Qualitative visualization and comparisons with EDITVAE are provided in Fig. 3. SPA-VAE achieved better segmentation results as, e.g. table legs and airplane wings are segmented by two similar

| Category | SPA-VAE | SPA-VAE-R | EDITVAE-R | EDITVAE |
|----------|---------|--------------|--------------|---------|
| Table | 0.068 | 0.073 | 0.044 | 0.042 |
| Chair | 0.065 | 0.047 | 0.044 | 0.047 |
| Airplane | 0.067 | 0.032 | 0.044 | 0.044 |

Table 2: JSD performance for resampled models denoted by the suffix -R.

parts with less part overlap. We generally found that, as observed in the figure, SPA-VAE generates 3D point clouds with more diverse styles, presumably because similar parts from the same object effectively augment the training data leading more detailed and diverse shape prototypes for the parts. For example, the stand and the bottoms of the tables are distinguished by more precise details in the fourth column of Fig. 3. Furthermore, SPA-VAE tends to avoid mismatched part styles, unlike *e.g.* the arms of the sofa chair generated by EDITVAE at the bottom-left of Fig. 3.

4.2 Completion

The way SPA-VAE explicitly learns similarity relationships between parts within an object provides a new mode of intelligent data-driven 3D shape completion. We now introduce two variants of SPA-VAE to demonstrate the strength of similarity in completion tasks. Different from recent learning-based completion methods, the demonstration merely uses ground-truth point clouds of complete objects during training, and incomplete point clouds in testing.

Completion by Reconstruction. As a baseline, completion can be achieved with a pretrained SPA-VAE model by simply encoding and decoding the incomplete point cloud. We denote this method by COMPLETION-R.

Completion by Similarity. We give a simple recipe for exploiting the parts-based self-similarity inferred by SPA-VAE. First we encode the incomplete point cloud using the same pretrained SPA-VAE model as before. We then extract the inferred poses, primitives, and the assignment matrix. We then assign each point of the incomplete point cloud to the nearest primitive. Finally, to fill in the missing region of the incomplete point cloud, we copy each input point x to each of the corresponding (zero or more) shared parts. This is achieved by transforming by $x \mapsto \mathcal{T}^{m'}((\mathcal{T}^m)^{-1}(x))$ where m and m' are the source and target part indices, respectively, yielding a completed point cloud. We denote this method by COMPLETION-S.

We simulate incomplete data with two corruptions. The CUT corruption removes all the data in a particular half-space of a certain part (using SHAPENET’s part labels), while the HOLE corruption removes the data inside an L^2 ball within a part. We only corrupt parts with shared (similar) counterparts. Further details of these corruption processes may be found in the supplementary materials. Visualizations of our completions of these corruptions are shown in Fig. 4. We also used the Chamfer Distance to measure the completion quality quantitatively as summarized in Fig. 5 and Appendix D Fig. 6. As we can see, COMPLETION-S

outperforms COMPLETION-R on both the CUT and HOLE tasks, in both the airplane and chair categories. In particular, COMPLETION-S is effective (that is, outperforms the UN-COMPLETED input point cloud) when ≈ 100 or more points are removed, whereas COMPLETION-R is effective in this sense only when ≈ 200 or more point are removed.

See Appendix C for the completion baseline comparison.

4.3 Ablation Studies and Measurements

Imbalanced Points Distribution The SPA-VAE model can lead to a non-uniform distribution of points per *semantic* part, because semantic parts (those corresponding to a fixed real-world definition such as the leg of a chair) tend to be segmented unequally into parts in the sense of the SPA-VAE disentanglement. This is part of a trade-off between the uniformity of the distribution of points per part, and the level of detail captured, since unbalanced segmentation can help to represent fine details by assigning smaller regions to geometrically complex parts yielding more points per unit of surface area. The *diversity loss* introduced by SPA-VAE helps to model fine details (see Fig. 3) but leads to imbalanced points distributions (see the supplementary for statistics). However, the JSD evaluation metric¹ penalizes non-uniform points distributions because the ground truth point clouds tend to be distributed uniformly, and so may not be suitable for evaluating models aiming at representing fine details more adaptively.

Here we propose a modification to SPA-VAE which reduces the impact of this imbalance on the JSD metric. SPA-VAE-R (and similarly the baseline EDITVAE-R) is defined by down-sampling the generated parts point cloud by a rate which is set for each part separately. The rate is chosen to match the mean number of points assigned to the corresponding parts in training. This yields a final output point cloud which is distributed more uniformly. As we can see in Tab. 2, the result is a better JSD performance, with SPA-VAE-R comparable to EDITVAE-R in terms of JSD.

Others See Appendix B for part self-similarity and semantic meaningfulness, as well as the ablation study on novel loss terms.

5 Conclusion and Limitation

We proposed SPA-VAE, which exploits parts-based self-similarity within the problem of parts-aware generation and completion. SPA-VAE effectively combines the training data from repeated parts of an object, by both segmenting shapes into parts (thereby augmenting the 3D points used for fitting) and explicitly modelling shapes with similar parts (ensuring part consistency). A limitation of our model is that, due to the naturally existence of self-symmetry within single parts, predicting pose may be challenging and potentially sensitive to noise, especially in the generation setting. We aim to improve this in future works.

¹The JSD metric typically used on SHAPENET approximates a point cloud by a distribution by quantizing points to a (voxel) grid, counting & normalizing to a probability distribution, and computing the Jensen-Shannon divergence measure between two distributions obtained this way.

A Notation Guide

| Symbol | Explanation |
|------------------------|--|
| \mathbf{X} | Input point cloud. |
| M_s | Number of latent candidate shapes. |
| $M_{\mathcal{T}}$ | Number of parts (and so part poses) in the assembled object. |
| \mathbf{A} | <i>Candidate shape to object part assignment matrix</i> $\in \{0, 1\}^{M_s \times M_{\mathcal{T}}}$. |
| z_g | <i>global</i> latent embedding vector |
| $z_{\mathcal{T}}$ | <i>transformation (pose)</i> latent embedding vector |
| z_s | <i>shape</i> latent embedding vector |
| \mathcal{T}^m | m -th canonical- to object-coordinate transform, for $m = 1, 2, \dots M_{\mathcal{T}}$. |
| $\tilde{\mathbf{Y}}^m$ | m -th candidate shape point cloud in canonical coordinates, for $m = 1, 2, \dots M_s$. |
| $\hat{\mathbf{Y}}^m$ | m -th part point cloud in canonical coordinates, for $m = 1, 2, \dots M_{\mathcal{T}}$, as selected by \mathbf{A} . |
| \mathbf{Y}^m | m -th part point cloud in object coordinates, for $m = 1, 2, \dots M_{\mathcal{T}}$, as transformed by \mathcal{T}^m . |
| $\tilde{\mathbf{P}}^m$ | m -th candidate shape primitive in canonical coordinates, for $m = 1, 2, \dots M_s$. |
| $\hat{\mathbf{P}}^m$ | m -th part primitive in canonical coordinates, for $m = 1, 2, \dots M_{\mathcal{T}}$, as selected by \mathbf{A} . |
| \mathbf{P}^m | m -th part primitive in object coordinates, for $m = 1, 2, \dots M_{\mathcal{T}}$, as transformed by \mathcal{T}^m . |
| ζ^m | $= \{\mathcal{T}^m, \hat{\mathbf{Y}}^m, \hat{\mathbf{P}}^m\}$, combined m -th part representation for $m = 1, 2, \dots M_{\mathcal{T}}$. |
| ζ | $= \bigcup_{m=1}^{M_{\mathcal{T}}} \zeta^m$ combined ζ^m . |
| $\tilde{\mathbf{P}}$ | $= \bigcup_{m=1}^{M_s} \tilde{\mathbf{P}}^m$ combined $\tilde{\mathbf{P}}^m$. |
| $\hat{\mathbf{P}}$ | $= \bigcup_{m=1}^{M_{\mathcal{T}}} \hat{\mathbf{P}}^m$ combined $\hat{\mathbf{P}}^m$. |
| \mathbf{P} | $= \bigcup_{m=1}^{M_{\mathcal{T}}} \mathbf{P}^m$ combined \mathbf{P}^m , the output set of superquadrics. |
| $\tilde{\mathbf{Y}}$ | $= \bigcup_{m=1}^{M_s} \tilde{\mathbf{Y}}^m$ combined $\tilde{\mathbf{Y}}^m$. |
| $\hat{\mathbf{Y}}$ | $= \bigcup_{m=1}^{M_{\mathcal{T}}} \hat{\mathbf{Y}}^m$ combined $\hat{\mathbf{Y}}^m$. |
| \mathbf{Y} | $= \bigcup_{m=1}^{M_{\mathcal{T}}} \mathbf{Y}^m$ combined \mathbf{Y}^m , the output point cloud. |

| | Mean Chamfer Distance | | | Min Chamfer Distance | | |
|----------|-----------------------|---------------|---------------|----------------------|---------------|---------------|
| Category | Airplane | Table | Chair | Airplane | Table | Chair |
| SPA-VAE | 0.0017 | 0.0064 | 0.0023 | 0.0012 | 1.3e-5 | 4.1e-5 |
| EDITVAE | 0.0267 | 0.0371 | 0.0251 | 0.0030 | 0.0199 | 0.0143 |

Table 3: Measurement of parts-based self-similarity.

| | MCD ↓ | | |
|---------------------------------|---------------|---------------|---------------|
| | Chair | Airplane | Table |
| EDITVAE | 0.0026 | 0.0016 | 0.0121 |
| SPA-VAE | 0.0058 | 0.0096 | 0.0146 |
| SPA-VAE-M | 0.0010 | 0.0009 | 0.0011 |
| NEURAL PARTS | 0.0032 | 0.0018 | 0.0063 |
| BSP-NET | 0.0102 | 0.0052 | 0.0124 |
| SPA-VAE-M - <i>d</i> | 0.0021 | 0.0015 | 0.0032 |
| SPA-VAE-M - <i>a</i> | 0.0024 | 0.0017 | 0.0028 |
| SPA-VAE-M - <i>d</i> - <i>a</i> | 0.0027 | 0.0013 | 0.0035 |

Table 4: Semantic Meaningfulness. Here -*d* and -*a* denote training SPA-VAE without the diversity loss \mathcal{L}_d and assignment loss \mathcal{L}_a , respectively.

B Ablation Studies and Measurements

Parts Self-Similarity and Semantic Meaningfulness *Self-similarity* could be measured by the mean or min of Chamfer distances of all pairs of generated parts in canonical position within a single point cloud. As shown in Tab. 3, SPA-VAE has smaller mean and min Chamfer distances compared with EDITVAE, indicating the discovery of self-similar parts.

In Tab. 4, we measure the *semantic meaningfulness* with MCD introduced in (Li, Liu, and Walder 2022). We compared the semantic meaningfulness with EDITVAE (Li, Liu, and Walder 2022), NEURAL PARTS (Paschalidou et al. 2021), and BSP-NET (Chen, Tagliasacchi, and Zhang 2020). We further propose SPA-VAE-M by merging self-similar parts as one, and then calculate MCD. As SPA-VAE-M strongly outperforms EDITVAE, we conclude that SPA-VAE discovers 3D shapes in a hierarchical manner, which is described below. First, it tends to segment 3D shapes by non-shared canonical shapes, whose segmentation is close to semantic ones (proved by good performance of SPA-VAE-M). Second, it further discovers self-similar parts within each discovered part type.

Ablations Study on Novel Loss Terms Recall that we introduced two novel loss terms as part of the SPA-VAE model, namely the diversity loss \mathcal{L}_d and the assignment loss \mathcal{L}_a . We confirmed their importance by removing one, the other, and both from our training optimization, yielding the quantitative results shown in Tab. 5.

C Compare with Completion Baselines

We compared COMPLETION-S with the State-of-the-art (SOTA) completion method (Zhang et al. 2021) by using

| Model | JSD ↓ | MMD-CD ↓ | MMD-EMD ↓ | COV-CD ↑ | COV-EMD ↑ |
|-------------------------------|--------------|---------------|--------------|-----------|-----------|
| SPA-VAE - <i>d</i> | 0.111 | 0.0018 | 0.022 | 44 | 17 |
| SPA-VAE - <i>a</i> | 0.109 | 0.0018 | 0.118 | 42 | 23 |
| SPA-VAE - <i>d</i> - <i>a</i> | 0.114 | 0.0018 | 0.033 | 43 | 17 |
| SPA-VAE | 0.068 | 0.0016 | 0.020 | 45 | 21 |

Table 5: Ablation study of our novel losses for the *table* category. Here -*d* and -*a* denote training SPA-VAE without the diversity loss \mathcal{L}_d and assignment loss \mathcal{L}_a , respectively.

their pre-trained model in our incomplete data set directly (“(Zhang et al. 2021) PRETRAIN”), and training their model with complete data and then applying to incomplete test data (“(Zhang et al. 2021) FAIR”), in order to maintain a fair comparison. We further introduced an ‘unfair’ setting in which we train the SOTA with complete and incomplete (cut 400 point as in Sec. 4.2) pairs directly (“(Zhang et al. 2021) - 400”). As the proposed SPA-VAE is designed purely using complete point clouds in training, “(Zhang et al. 2021) - 400” taking advantage of observing the incomplete data. All the above models are tested by completing table point clouds cutted by different number of points. As in Tab. 6, COMPLETION-S outperforms “(Zhang et al. 2021) PRETRAIN” and “(Zhang et al. 2021) - 400”, while “(Zhang et al. 2021) FAIR” failed when only tuning with complete data. As SOTA completion methods rely heavily on training with both complete and incomplete point clouds pairs, SPA-VAE contributes as 1) relevant and diverse incomplete data may be hard to obtain in the real world. 2) transferred models may could not be adopted well. 3) self similarities may allow accurate completion of parts not seen in training yet observed (in a complete self similar part of) the input.

D More Completion Corruption Results

See Fig 6 for more completion corruption results.

E Completion Details

E.1 Completion Methods

Two completion methods (COMPLETION-R and COMPLETION-S) are introduced in Sec. 4.2 of the main paper, here we further provide the diagram of Fig. 7.

E.2 Corruption Details

CUT corruption is defined by removing all points in a particular half-space of a certain part for which a similar counterpart exists. The half-space is defined by decreasingly sorting points according the weighted sum of (x, y, z) values and then removing the top K points, with fixed uniformly random weights.

HOLE corruption is defined by removing a “ball” from a certain part whose similar counterpart exists. The ball is defined by a center point randomly sampled from the part’s point cloud, together with K nearest neighborhoods of it. To distinguish with CUT, we further sample the center point by first sorting all parts points as in CUT, and then selecting the point at the K -th rank, to make it more likely that it is interior to the shape.

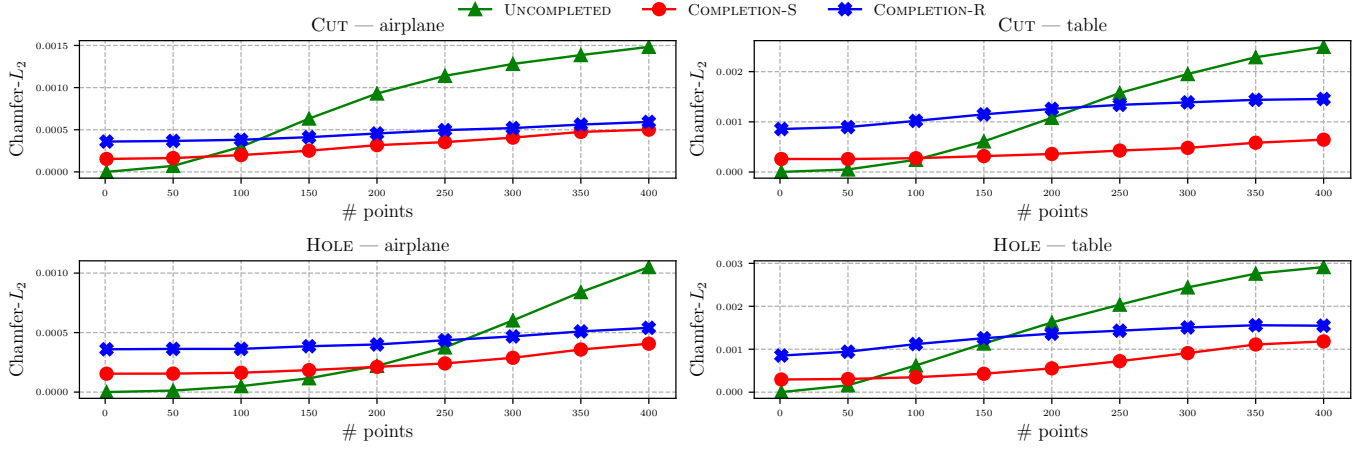


Figure 6: Completion of CUT and HOLE input point cloud corruptions, for the airplane and table categories. *Horizontal*: the number of points removed from ground truth point cloud. *Vertical*: the Chamfer distance between the ground truth point cloud and the UNCOMPLETED one (green), or the completed one using either the COMPLETION-R (blue), or COMPLETION-S (red) methods.

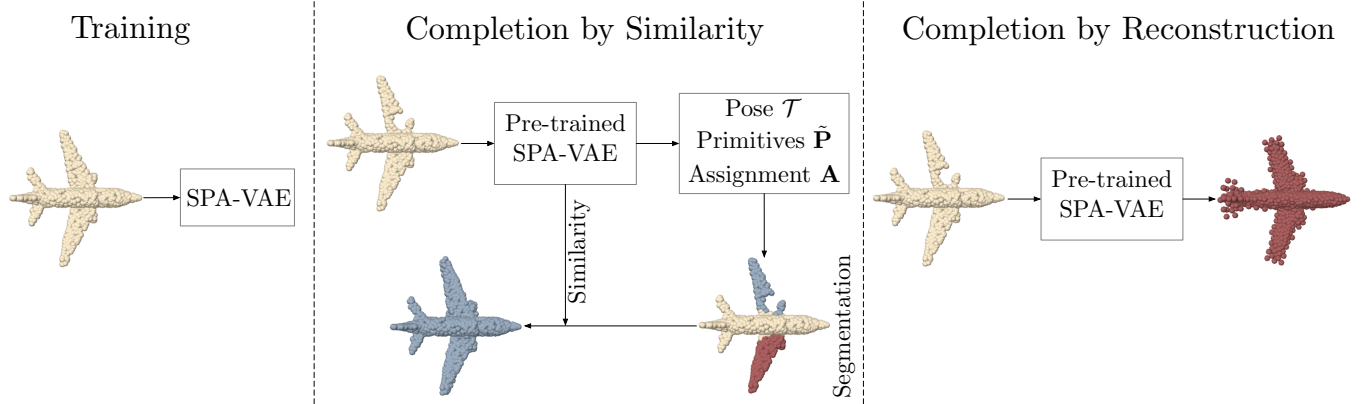


Figure 7: Visualising completion. *Left*: SPA-VAE is first pre-trained with complete data. *Middle*: Completion by similarity (COMPLETION-S) is achieved by first inferring an unsupervised segmentation for the incomplete point cloud input using the pre-trained SPA-VAE, and then copying points using the obtained similarity. *Right*: Completion by reconstruction (COMPLETION-R) is achieved by feeding the incomplete point cloud input into the pre-trained SPA-VAE.

| Number | 1 | 50 | 100 | 150 | 200 | 250 | 300 | 350 | 400 |
|------------------------------|----------------------|----------------------|------------|------------|------------|------------|------------|------------|------------|
| UNCOMPLETED | $\approx \mathbf{0}$ | $\approx \mathbf{0}$ | 2.4 | 6.1 | 10.8 | 15.7 | 19.5 | 22.9 | 24.9 |
| (Zhang et al. 2021) PRETRAIN | 9.3 | 9.0 | 9.7 | 10.1 | 11.2 | 10.0 | 10.7 | 11.8 | 11.5 |
| COMPLETION-S | 2.6 | 2.6 | 2.7 | 3.2 | 3.6 | 4.3 | 4.8 | 5.8 | 6.4 |
| (Zhang et al. 2021) - 400 | 7.2 | 6.9 | 7.9 | 8.3 | 9.1 | 8.7 | 9.7 | 10.5 | 9.5 |
| (Zhang et al. 2021) FAIR | 821.2 | 823.0 | 794.4 | 789.5 | 839.5 | 841.3 | 810.3 | 839.9 | 860.8 |

Table 6: Comparison with completion baseline in terms of mean Chamfer distance $\times 10^4$. Category: table, corruption: CUT

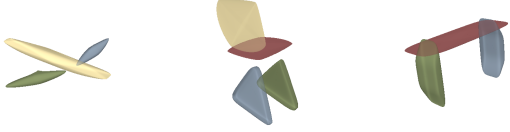


Figure 8: Generated primitives. Each part/primitive is highlighted by different color. In all categories, blue and green parts are self-similar parts with shared shape but separate poses.

F Visualization of Generated Primitives

The visualization of generated primitives is shown in Fig. 8, which is assembled from outputs (pose \mathcal{T} , canonical candidate primitive \tilde{P} , and assignment matrix A) of a pre-trained SPA-VAE, by sampling from standard Gaussian prior. See Sec. 3 in the main paper for details.

G Another View of Similar Parts Assignment

We performed similar parts assignment by defining the assignment matrix A , which selects shapes (points and primitives) according to Eq. 4 in the main paper. While the main paper’s derivation is clear, here we provide another view of similar parts assignment based on the n -mode product (Kolda and Bader 2009), to show that the proposed similarity is differentiable, effective and neural-network-friendly.

We take M_s number of *canonical candidate* point clouds $\tilde{Y}^m \in \mathbf{R}^{N_p \times 3}$ outputted by point decoders, and concatenate to a tensor $\tilde{Y} \in \mathbf{R}^{N_p \times 3 \times M_s}$. Then the selection by assignment matrix $A \in \mathbf{R}^{M_s \times M_{\mathcal{T}}}$ is easily expressed as

$$\hat{Y} = \tilde{Y} \times_3 A^T, \quad (14)$$

here \times_3 is 3-mode product. And all point clouds \hat{Y}^m in parts ζ^m concatenated together to form $\hat{Y} \in \mathbf{R}^{N_p \times 3 \times M_{\mathcal{T}}}$. The column of assignment matrix A_j (row of A^T) is a one hot vector, and its dot production with respect to the last dimension of \hat{Y} (number of shapes) simply selects one of M_s shapes, which matches Sec. 2.5 in (Kolda and Bader 2009). Finally, parts point clouds are transformed and composed to form the output point cloud $Y \in \mathbf{R}^{N \times 3}$ by way of the parts-based pose transformation function \mathcal{T}^m and (inverse) vectorization operation as in Sec. 3.3 of the main paper.

Similarly, primitives may be represented by first sampling angles η and ω , then transforming to the primitives surface with Eq. 3 in the main paper. Thus, *canonical candidate*

| Model | Category | Number of Points Per Part | | | | $SDev$ |
|----------|----------|---------------------------|------------|------------|------------|------------|
| EDITVAE | Chair | 714 | 489 | 445 | 400 | 121 |
| SPA-VAE | | 756 | 737 | 284 | 271 | 235 |
| BALANCED | | 512 | 512 | 512 | 512 | 0 |
| EDITVAE | Table | 974 | 569 | 505 | - | 208 |
| SPA-VAE | | 1234 | 409 | 405 | - | 390 |
| BALANCED | | 683 | 683 | 682 | - | 0 |
| EDITVAE | Airplane | 813 | 735 | 500 | - | 133 |
| SPA-VAE | | 1069 | 515 | 464 | - | 274 |
| BALANCED | | 683 | 683 | 682 | - | 0 |

Table 7: Per parts points distribution. Here $SDev$ denotes the standard deviation of the number of points per part, smaller means closer to uniform points distribution. BALANCED denotes the ideally uniformly distributed points.

primitives \tilde{P}^m may be represented as a set of points on its surface in $\mathbf{R}^{N_r \times 3}$, with N_r the number of sampled angles (surface points). All canonical candidate primitives could be similarly concatenated to form $\tilde{P} \in \mathbf{R}^{N_r \times 3 \times M_s}$. Same as point clouds \tilde{Y} , the selection of canonical primitives may be represented as

$$\hat{P} = \tilde{P} \times_3 A^T, \quad (15)$$

here $\hat{P} \in \mathbf{R}^{N_r \times 3 \times M_{\mathcal{T}}}$, which could be separated as primitives \hat{P}^m into parts ζ^m , to finally form the surface-point version of the primitives P by way of poses \mathcal{T} and (inverse) vectorization as for the point clouds.

H Imbalanced Points Distribution Statistics

Here we demonstrate that SPA-VAE generates an imbalanced points distribution, which helps to model fine details of point clouds as described in Sec. 4.3 of the main paper. The statistics of points distribution are listed in Tab. 7. Here we assume that ground-truth point clouds used in training and testing have points distributed uniformly. Ideally, the uniform points distribution in ground-truth point clouds is guaranteed by: 1) each part’s point cloud contains the same number of points, and 2) points are distributed uniformly within parts. The former is reflected by ideally BALANCED parts generation in Tab. 7 and the latter is achieved by points decoders with the help of the Chamfer distance loss, which is not covered further here.

As the parts are designed to output equal numbers of points per points decoder, and imbalanced distribution arises

from assigning points in the ground truth input to the nearest part / primitive in reconstruction, for both the SPA-VAE and EDITVAE, in line with Tab. 7. Because it reflects how much the parts-aware generations violate the above rule (1) — each generated/segmented parts tend to contain various points number when mapped to the ground-truth point clouds. Compared with EDITVAE, SPA-VAE outputs parts whose assigned ground-truth points number shows a higher *standard deviation*. Compared with the ideal represented by BALANCED whose parts segment the ground truth point cloud equally, high variance means parts generated by SPA-VAE tend to contain an imbalanced number of points in the ground truth point cloud, as each part is designed to output an equal number of parts in generation. Thus, the higher standard deviation exhibited by SPA-VAE indicates a more imbalanced points distribution, and so potentially a more detailed representation but worse JSD performance.

I Implementation Details

Generation Evaluation Metrics This paper adopts the same evaluation metrics as in (Achlioptas et al. 2018; Shu, Park, and Kwon 2019; Li, Liu, and Walder 2022). To be self-contained, we present their definitions below. Assume we have a set of n generated point clouds $\mathbf{Y} = \{\mathbf{Y}_i\}$ for $i \in \{1, \dots, n\}$ and a set of m ground-truth point clouds $\mathbf{X} = \{\mathbf{X}_j\}$ for $j \in \{1, \dots, m\}$.

- *Coverage (COV)* is defined as the fraction of ground-truth point clouds \mathbf{X} which is the closest one for any generated point cloud \mathbf{Y}_i

$$\text{COV}(\mathbf{X}, \mathbf{Y}) = \frac{|\mathbf{X}'|}{|\mathbf{X}|} \quad (16)$$

$$\mathbf{X}' = \{\mathbf{X}_j | \arg \max_{\mathbf{X}_j \in \mathbf{X}} -d(\mathbf{X}_j, \mathbf{Y}_i) \text{ for } i \in \{1, \dots, n\}\}$$

- *Minimum Matching Distance (MMD)* is defined as the mean of minimum distance for each ground-truth point cloud \mathbf{X}_j with respect to any generated point cloud \mathbf{Y}_i

$$\text{MMD}(\mathbf{X}, \mathbf{Y}) = \frac{1}{m} \sum_{j=1}^m \min_{\mathbf{Y}_i \in \mathbf{Y}} d(\mathbf{X}_j, \mathbf{Y}_i) \quad (17)$$

- *Jensen-Shannon Divergence (JSD)* is defined to measure the degree to which the point in axis-aligned generated point clouds \mathbf{Y} tends to appear at the similar position as in the ground-truth one \mathbf{X} . As in (Achlioptas et al. 2018) JSD is defined by a canonical voxel grid in the ambient space. With the empirical distribution (counting the number of *all* points within voxels) of the point clouds set defined as \mathbf{P} , we have

$$\text{JSD}(\mathbf{P}_\mathbf{X} \parallel \mathbf{P}_\mathbf{Y}) = \frac{1}{2} D(\mathbf{P}_\mathbf{X} \parallel \mathbf{M}) + \frac{1}{2} D(\mathbf{P}_\mathbf{Y} \parallel \mathbf{M}), \quad (18)$$

where $\mathbf{M} = \frac{1}{2}(\mathbf{P}_\mathbf{X} + \mathbf{P}_\mathbf{Y})$ and $D(\cdot \parallel \cdot)$ is the KL-divergence (Kullback and Leibler 1951).

For the *COV* and *MMD*, $d(\cdot, \cdot)$ is the distance between two point clouds, which could be defined as Chamfer distance and Earth Mover distance (Rubner, Tomasi, and Guibas 2000). The formal definition of the above two distances could be found in the Sec. 2 of (Achlioptas et al. 2018).

Network Architecture We adopt the same network architecture as (Li, Liu, and Walder 2022) except for the addition of a fully connected layer Δ_θ used in the Gumbel softmax estimation of Sec. 3.2 of the main paper. In particular, the encoder is based on POINTNET (Qi et al. 2017), with TREEGAN’s generator as point decoders (Shu, Park, and Kwon 2019), and fully connected layers as primitive decoders (Paschalidou, Ulusoy, and Geiger 2019). We further set τ in the Gumbel softmax estimator of the main paper Eq. 6 to 1, which yields a smooth estimator with small gradient.

Loss Details See (Li, Liu, and Walder 2022; Paschalidou, Ulusoy, and Geiger 2019) and their supplementary for the details of the points distance \mathcal{L}_p , primitives to points distance \mathcal{L}_r , and overlapping loss \mathcal{L}_o . We adopt Eq. 8 rather than Eq. 11 in (Paschalidou, Ulusoy, and Geiger 2019) for calculating the directed distance from points to primitives as SPA-VAE omits the existence probability otherwise associated with each primitive, in order to simplify the model. Further, we set s in overlapping loss (Eq. 10 in main paper) as the hyperparameter to control the overlapping or disjointedness among primitives. Specifically, $s > 1$ will promote disjointedness as the value of smoothed inside-outside indicator function (Solina and Bajcsy 1990) tends to greater than 1, with $s = 1$ on the surface, and $s < 1$ for overlaps. We set $c_1 = 4$ in the diversity loss, to achieve a close loss and gradient value compared with other losses, while keeping away from the convergence.

The weight of losses is assigned to $\omega_o = 1e - 6$, $\omega_d = 1e - 6$, $\omega_a = 0.1$, and $s = 1.3$ in table; $\omega_o = 2e - 3$, $\omega_d = 3e - 3$, $\omega_a = 0.1$, and $s = 1.5$ in chair; $\omega_o = 1e - 3$, $\omega_d = 1e - 5$, $\omega_a = 0.1$, and $s = 1$ in airplane.

Miscellaneous Details The model is implemented using PyTorch (Paszke et al. 2017) built on Ubuntu 16.04, and trained mainly on one GeForce RTX 3090 and one GeForce RTX 2080 TI. Roughly 5 Gigabytes of GPU memory is allocated, but this depends on the batch size, number of parts, and ShapeNet category. The selection of the number of parts roughly matches the choice in (Li, Liu, and Walder 2022), except for the chair category whose parts number is 3 in EDITVAE and 4 in SPA-VAE, as the latter further separates the legs into two similar parts.

References

- Achlioptas, P.; Diamanti, O.; Mitliagkas, I.; and Guibas, L. 2018. Learning representations and generative models for 3d point clouds. In *International conference on machine learning*, 40–49. PMLR.
- Barr, A. H. 1987. Global and local deformations of solid primitives. In *Readings in Computer Vision*, 661–670. Elsevier.
- Brock, A.; Donahue, J.; and Simonyan, K. 2018. Large scale GAN training for high fidelity natural image synthesis. *arXiv preprint arXiv:1809.11096*.
- Burgess, C. P.; Higgins, I.; Pal, A.; Matthey, L.; Watters, N.; Desjardins, G.; and Lerchner, A. 2018. Understanding disentangling in β -VAE. *arXiv preprint arXiv:1804.03599*.

- Cai, R.; Yang, G.; Averbuch-Elor, H.; Hao, Z.; Belongie, S.; Snavely, N.; and Hariharan, B. 2020. Learning gradient fields for shape generation. In *Computer Vision–ECCV 2020: 16th European Conference, Glasgow, UK, August 23–28, 2020, Proceedings, Part III 16*, 364–381. Springer.
- Chang, A. X.; Funkhouser, T.; Guibas, L.; Hanrahan, P.; Huang, Q.; Li, Z.; Savarese, S.; Savva, M.; Song, S.; Su, H.; et al. 2015. Shapenet: An information-rich 3d model repository. *arXiv preprint arXiv:1512.03012*.
- Chen, X.; Chen, B.; and Mitra, N. J. 2019. Unpaired point cloud completion on real scans using adversarial training. *arXiv preprint arXiv:1904.00069*.
- Chen, Z.; Tagliasacchi, A.; and Zhang, H. 2020. Bsp-net: Generating compact meshes via binary space partitioning. In *Proceedings of the IEEE/CVF Conference on Computer Vision and Pattern Recognition*, 45–54.
- Chen, Z.; Yin, K.; Fisher, M.; Chaudhuri, S.; and Zhang, H. 2019. BAE-NET: branched autoencoder for shape co-segmentation. In *Proceedings of the IEEE/CVF International Conference on Computer Vision*, 8490–8499.
- Deng, B.; Genova, K.; Yazdani, S.; Bouaziz, S.; Hinton, G.; and Tagliasacchi, A. 2020. Cvxnet: Learnable convex decomposition. In *Proceedings of the IEEE/CVF Conference on Computer Vision and Pattern Recognition*, 31–44.
- Diao, H.; Zhang, Y.; Ma, L.; and Lu, H. 2021. Similarity Reasoning and Filtration for Image-Text Matching. Technical report, Technical Report.
- Dubrovina, A.; Xia, F.; Achlioptas, P.; Shalah, M.; Groscot, R.; and Guibas, L. J. 2019. Composite shape modeling via latent space factorization. In *Proceedings of the IEEE/CVF International Conference on Computer Vision*, 8140–8149.
- Gal, R.; Bermanno, A.; Zhang, H.; and Cohen-Or, D. 2021. MRGAN: Multi-Rooted 3D Shape Representation Learning With Unsupervised Part Disentanglement. In *Proceedings of the IEEE/CVF International Conference on Computer Vision*, 2039–2048.
- Genova, K.; Cole, F.; Sud, A.; Sarna, A.; and Funkhouser, T. 2020. Local deep implicit functions for 3d shape. In *Proceedings of the IEEE/CVF Conference on Computer Vision and Pattern Recognition*, 4857–4866.
- Genova, K.; Cole, F.; Vlastic, D.; Sarna, A.; Freeman, W. T.; and Funkhouser, T. 2019. Learning shape templates with structured implicit functions. In *Proceedings of the IEEE/CVF International Conference on Computer Vision*, 7154–7164.
- Gong, B.; Nie, Y.; Lin, Y.; Han, X.; and Yu, Y. 2021. ME-PCN: Point Completion Conditioned on Mask Emptiness. In *Proceedings of the IEEE/CVF International Conference on Computer Vision*, 12488–12497.
- Goodfellow, I.; Pouget-Abadie, J.; Mirza, M.; Xu, B.; Warde-Farley, D.; Ozair, S.; Courville, A.; and Bengio, Y. 2014. Generative adversarial nets. *Advances in neural information processing systems*, 27.
- Gu, J.; Ma, W.-C.; Manivasagam, S.; Zeng, W.; Wang, Z.; Xiong, Y.; Su, H.; and Urtasun, R. 2020. Weakly-supervised 3D Shape Completion in the Wild. In *Computer Vision–ECCV 2020: 16th European Conference, Glasgow, UK, August 23–28, 2020, Proceedings, Part V 16*, 283–299. Springer.
- Higgins, I.; Matthey, L.; Pal, A.; Burgess, C.; Glorot, X.; Botvinick, M.; Mohamed, S.; and Lerchner, A. 2016. beta-vae: Learning basic visual concepts with a constrained variational framework.
- Huang, J.; and You, S. 2012. Point cloud matching based on 3D self-similarity. In *2012 IEEE Computer Society Conference on Computer Vision and Pattern Recognition Workshops*, 41–48. IEEE.
- Huang, T.; Zou, H.; Cui, J.; Yang, X.; Wang, M.; Zhao, X.; Zhang, J.; Yuan, Y.; Xu, Y.; and Liu, Y. 2021. RFNet: Recurrent Forward Network for Dense Point Cloud Completion. In *Proceedings of the IEEE/CVF International Conference on Computer Vision*, 12508–12517.
- Hui, L.; Xu, R.; Xie, J.; Qian, J.; and Yang, J. 2020. Progressive point cloud deconvolution generation network. In *Computer Vision–ECCV 2020: 16th European Conference, Glasgow, UK, August 23–28, 2020, Proceedings, Part XV 16*, 397–413. Springer.
- Jang, E.; Gu, S.; and Poole, B. 2016. Categorical reparameterization with gumbel-softmax. *arXiv preprint arXiv:1611.01144*.
- Karras, T.; Laine, S.; and Aila, T. 2019. A style-based generator architecture for generative adversarial networks. In *Proceedings of the IEEE/CVF Conference on Computer Vision and Pattern Recognition*, 4401–4410.
- Kim, H.; Lee, H.; Kang, W. H.; Lee, J. Y.; and Kim, N. S. 2020. Softflow: Probabilistic framework for normalizing flow on manifolds. *Advances in Neural Information Processing Systems*, 33.
- Kingma, D. P.; and Ba, J. 2014. Adam: A method for stochastic optimization. *arXiv preprint arXiv:1412.6980*.
- Kingma, D. P.; and Welling, M. 2013. Auto-encoding variational bayes. *arXiv preprint arXiv:1312.6114*.
- Klokov, R.; Boyer, E.; and Verbeek, J. 2020. Discrete point flow networks for efficient point cloud generation. In *Computer Vision–ECCV 2020: 16th European Conference, Glasgow, UK, August 23–28, 2020, Proceedings, Part XXIII 16*, 694–710. Springer.
- Kolda, T. G.; and Bader, B. W. 2009. Tensor decompositions and applications. *SIAM review*, 51(3): 455–500.
- Kullback, S.; and Leibler, R. A. 1951. On information and sufficiency. *The annals of mathematical statistics*, 22(1): 79–86.
- Kwon, H.; Kim, M.; Kwak, S.; and Cho, M. 2021. Learning self-similarity in space and time as generalized motion for video action recognition. In *Proceedings of the IEEE/CVF International Conference on Computer Vision*, 13065–13075.
- Li, R.; Li, X.; Hui, K.-H.; and Fu, C.-W. 2021. SP-GAN: sphere-guided 3D shape generation and manipulation. *ACM Transactions on Graphics (TOG)*, 40(4): 1–12.

- Li, S.; Liu, M.; and Walder, C. 2022. EditVAE: Unsupervised Part-Aware Controllable 3D Point Cloud Shape Generation. In *Proceedings of the AAAI Conference on Artificial Intelligence*.
- Luo, S.; and Hu, W. 2021. Diffusion probabilistic models for 3d point cloud generation. In *Proceedings of the IEEE/CVF Conference on Computer Vision and Pattern Recognition*, 2837–2845.
- Maddison, C. J.; Mnih, A.; and Teh, Y. W. 2016. The concrete distribution: A continuous relaxation of discrete random variables. *arXiv preprint arXiv:1611.00712*.
- Mishra, S.; Zhang, Z.; Shen, Y.; Kumar, R.; Saligrama, V.; and Plummer, B. 2021. Effectively Leveraging Attributes for Visual Similarity. In *Proceedings of the IEEE/CVF Conference on Computer Vision and Pattern Recognition*, 3904–3909.
- Mitra, N. J.; Guibas, L. J.; and Pauly, M. 2006. Partial and approximate symmetry detection for 3d geometry. *ACM Transactions on Graphics (TOG)*, 25(3): 560–568.
- Mitra, N. J.; Pauly, M.; Wand, M.; and Ceylan, D. 2013. Symmetry in 3d geometry: Extraction and applications. In *Computer Graphics Forum*, volume 32, 1–23. Wiley Online Library.
- Mo, K.; Guerrero, P.; Yi, L.; Su, H.; Wonka, P.; Mitra, N.; and Guibas, L. J. 2019. Structrenet: Hierarchical graph networks for 3d shape generation. *arXiv preprint arXiv:1908.00575*.
- Mo, K.; Wang, H.; Yan, X.; and Guibas, L. 2020. PT2PC: Learning to generate 3d point cloud shapes from part tree conditions. In *European Conference on Computer Vision*, 683–701. Springer.
- Nash, C.; and Williams, C. K. 2017. The shape variational autoencoder: A deep generative model of part-segmented 3D objects. In *Computer Graphics Forum*, volume 36, 1–12. Wiley Online Library.
- Nie, Y.; Lin, Y.; Han, X.; Guo, S.; Chang, J.; Cui, S.; and Zhang, J. J. 2020. Skeleton-bridged point completion: From global inference to local adjustment. *arXiv preprint arXiv:2010.07428*.
- Paschalidou, D.; Gool, L. V.; and Geiger, A. 2020. Learning unsupervised hierarchical part decomposition of 3d objects from a single rgb image. In *Proceedings of the IEEE/CVF Conference on Computer Vision and Pattern Recognition*, 1060–1070.
- Paschalidou, D.; Katharopoulos, A.; Geiger, A.; and Fidler, S. 2021. Neural Parts: Learning expressive 3D shape abstractions with invertible neural networks. In *Proceedings of the IEEE/CVF Conference on Computer Vision and Pattern Recognition*, 3204–3215.
- Paschalidou, D.; Ulusoy, A. O.; and Geiger, A. 2019. Superquadrics revisited: Learning 3d shape parsing beyond cuboids. In *Proceedings of the IEEE/CVF Conference on Computer Vision and Pattern Recognition*, 10344–10353.
- Paszke, A.; Gross, S.; Chintala, S.; Chanan, G.; Yang, E.; DeVito, Z.; Lin, Z.; Desmaison, A.; Antiga, L.; and Lerer, A. 2017. Automatic differentiation in pytorch.
- Pauly, M.; Mitra, N. J.; Wallner, J.; Pottmann, H.; and Guibas, L. J. 2008. Discovering structural regularity in 3D geometry. In *ACM SIGGRAPH 2008 papers*, 1–11.
- Podolak, J.; Shilane, P.; Golovinskiy, A.; Rusinkiewicz, S.; and Funkhouser, T. 2006. A planar-reflective symmetry transform for 3D shapes. In *ACM SIGGRAPH 2006 Papers*, 549–559.
- Postels, J.; Liu, M.; Spezialetti, R.; Van Gool, L.; and Tombari, F. 2021. Go with the Flows: Mixtures of Normalizing Flows for Point Cloud Generation and Reconstruction. *arXiv preprint arXiv:2106.03135*.
- Qi, C. R.; Su, H.; Mo, K.; and Guibas, L. J. 2017. Pointnet: Deep learning on point sets for 3d classification and segmentation. In *Proceedings of the IEEE conference on computer vision and pattern recognition*, 652–660.
- Rezende, D. J.; Mohamed, S.; and Wierstra, D. 2014. Stochastic Backpropagation and Approximate Inference in Deep Generative Models. In Xing, E. P.; and Jebara, T., eds., *Proceedings of the 31st International Conference on Machine Learning*, volume 32 of *Proceedings of Machine Learning Research*, 1278–1286. Beijing, China: PMLR.
- Rubner, Y.; Tomasi, C.; and Guibas, L. J. 2000. The earth mover’s distance as a metric for image retrieval. *International journal of computer vision*, 40(2): 99–121.
- Schor, N.; Katzir, O.; Zhang, H.; and Cohen-Or, D. 2019. Componet: Learning to generate the unseen by part synthesis and composition. In *Proceedings of the IEEE/CVF International Conference on Computer Vision*, 8759–8768.
- Seo, A.; Shim, W.; and Cho, M. 2021. Learning to Discover Reflection Symmetry via Polar Matching Convolution. In *Proceedings of the IEEE/CVF International Conference on Computer Vision*, 1285–1294.
- Shu, D. W.; Park, S. W.; and Kwon, J. 2019. 3d point cloud generative adversarial network based on tree structured graph convolutions. In *Proceedings of the IEEE/CVF International Conference on Computer Vision*, 3859–3868.
- Sipiran, I.; Gregor, R.; and Schreck, T. 2014. Approximate symmetry detection in partial 3d meshes. In *Computer Graphics Forum*, volume 33, 131–140. Wiley Online Library.
- Solina, F.; and Bajcsy, R. 1990. Recovery of parametric models from range images: The case for superquadrics with global deformations. *IEEE transactions on pattern analysis and machine intelligence*, 12(2): 131–147.
- Stutz, D.; and Geiger, A. 2018. Learning 3d shape completion from laser scan data with weak supervision. In *Proceedings of the IEEE Conference on Computer Vision and Pattern Recognition*, 1955–1964.
- Sun, C.-Y.; Zou, Q.-F.; Tong, X.; and Liu, Y. 2019. Learning adaptive hierarchical cuboid abstractions of 3d shape collections. *ACM Transactions on Graphics (TOG)*, 38(6): 1–13.
- Sung, M.; Kim, V. G.; Angst, R.; and Guibas, L. 2015. Data-driven structural priors for shape completion. *ACM Transactions on Graphics (TOG)*, 34(6): 1–11.
- Tchapmi, L. P.; Kosaraju, V.; Rezatofighi, H.; Reid, I.; and Savarese, S. 2019. Topnet: Structural point cloud decoder.

- In *Proceedings of the IEEE/CVF Conference on Computer Vision and Pattern Recognition*, 383–392.
- Thrun, S.; and Wegbreit, B. 2005. Shape from symmetry. In *Tenth IEEE International Conference on Computer Vision (ICCV'05) Volume 1*, volume 2, 1824–1831. IEEE.
- Tulsiani, S.; Su, H.; Guibas, L. J.; Efros, A. A.; and Malik, J. 2017. Learning shape abstractions by assembling volumetric primitives. In *Proceedings of the IEEE Conference on Computer Vision and Pattern Recognition*, 2635–2643.
- Valsesia, D.; Fracastoro, G.; and Magli, E. 2018. Learning localized generative models for 3d point clouds via graph convolution. In *International conference on learning representations*.
- Walder, C.; and Kim, D. 2018a. Neural Dynamic Programming for Musical Self Similarity. In Dy, J.; and Krause, A., eds., *Proceedings of the 35th International Conference on Machine Learning*, volume 80 of *Proceedings of Machine Learning Research*, 5105–5113. PMLR.
- Walder, C.; and Kim, D. 2018b. Neural dynamic programming for musical self similarity. In *International Conference on Machine Learning*, 5105–5113. PMLR.
- Wang, X.; Ang, M. H.; and Lee, G. H. 2021. Voxel-based Network for Shape Completion by Leveraging Edge Generation. In *Proceedings of the IEEE/CVF International Conference on Computer Vision*, 13189–13198.
- Wang, X.; Ang Jr, M. H.; and Lee, G. H. 2020a. Cascaded refinement network for point cloud completion. In *Proceedings of the IEEE/CVF Conference on Computer Vision and Pattern Recognition*, 790–799.
- Wang, X.; Ang Jr, M. H.; and Lee, G. H. 2020b. A Self-supervised Cascaded Refinement Network for Point Cloud Completion. *arXiv preprint arXiv:2010.08719*.
- Wen, C.; Yu, B.; and Tao, D. 2021. Learning Progressive Point Embeddings for 3D Point Cloud Generation. In *Proceedings of the IEEE/CVF Conference on Computer Vision and Pattern Recognition*, 10266–10275.
- Wen, X.; Han, Z.; Cao, Y.-P.; Wan, P.; Zheng, W.; and Liu, Y.-S. 2021a. Cycle4completion: Unpaired point cloud completion using cycle transformation with missing region coding. In *Proceedings of the IEEE/CVF Conference on Computer Vision and Pattern Recognition*, 13080–13089.
- Wen, X.; Xiang, P.; Han, Z.; Cao, Y.-P.; Wan, P.; Zheng, W.; and Liu, Y.-S. 2021b. Pmp-net: Point cloud completion by learning multi-step point moving paths. In *Proceedings of the IEEE/CVF Conference on Computer Vision and Pattern Recognition*, 7443–7452.
- Wu, R.; Chen, X.; Zhuang, Y.; and Chen, B. 2020. Multimodal shape completion via conditional generative adversarial networks. In *Computer Vision—ECCV 2020: 16th European Conference, Glasgow, UK, August 23–28, 2020, Proceedings, Part IV 16*, 281–296. Springer.
- Wu, S.; Rupperecht, C.; and Vedaldi, A. 2020. Unsupervised learning of probably symmetric deformable 3d objects from images in the wild. In *Proceedings of the IEEE/CVF Conference on Computer Vision and Pattern Recognition*, 1–10.
- Xiang, P.; Wen, X.; Liu, Y.-S.; Cao, Y.-P.; Wan, P.; Zheng, W.; and Han, Z. 2021. Snowflakenet: Point cloud completion by snowflake point deconvolution with skip-transformer. In *Proceedings of the IEEE/CVF International Conference on Computer Vision*, 5499–5509.
- Xiao, T.; Reed, C. J.; Wang, X.; Keutzer, K.; and Darrell, T. 2021. Region similarity representation learning. *arXiv preprint arXiv:2103.12902*.
- Xie, C.; Wang, C.; Zhang, B.; Yang, H.; Chen, D.; and Wen, F. 2021. Style-based Point Generator with Adversarial Rendering for Point Cloud Completion. In *Proceedings of the IEEE/CVF Conference on Computer Vision and Pattern Recognition*, 4619–4628.
- Xie, H.; Yao, H.; Zhou, S.; Mao, J.; Zhang, S.; and Sun, W. 2020. Grnet: Gridding residual network for dense point cloud completion. In *European Conference on Computer Vision*, 365–381. Springer.
- Xu, Y.; Fan, T.; Yuan, Y.; and Singh, G. 2020. Ladybird: Quasi-monte carlo sampling for deep implicit field based 3d reconstruction with symmetry. In *European Conference on Computer Vision*, 248–263. Springer.
- Yang, G.; Huang, X.; Hao, Z.; Liu, M.-Y.; Belongie, S.; and Hariharan, B. 2019a. Pointflow: 3d point cloud generation with continuous normalizing flows. In *Proceedings of the IEEE/CVF International Conference on Computer Vision*, 4541–4550.
- Yang, J.; Zhang, Q.; Ni, B.; Li, L.; Liu, J.; Zhou, M.; and Tian, Q. 2019b. Modeling point clouds with self-attention and gumbel subset sampling. In *Proceedings of the IEEE/CVF Conference on Computer Vision and Pattern Recognition*, 3323–3332.
- Yang, K.; and Chen, X. 2021. Unsupervised learning for cuboid shape abstraction via joint segmentation from point clouds. *ACM Transactions on Graphics (TOG)*, 40(4): 1–11.
- Yang, X.; Wu, Y.; Zhang, K.; and Jin, C. 2021. CPCGAN: A Controllable 3D Point Cloud Generative Adversarial Network with Semantic Label Generating. In *Proceedings of the AAAI Conference on Artificial Intelligence*, volume 35, 3154–3162.
- Yoon, S.; Kang, W. Y.; Jeon, S.; Lee, S.; Han, C.; Park, J.; and Kim, E.-S. 2020. Image-to-Image Retrieval by Learning Similarity between Scene Graphs. *arXiv preprint arXiv:2012.14700*.
- Yuan, W.; Khot, T.; Held, D.; Mertz, C.; and Hebert, M. 2018. Pcn: Point completion network. In *2018 International Conference on 3D Vision (3DV)*, 728–737. IEEE.
- Zhang, J.; Chen, X.; Cai, Z.; Pan, L.; Zhao, H.; Yi, S.; Yeo, C. K.; Dai, B.; and Loy, C. C. 2021. Unsupervised 3D Shape Completion through GAN Inversion. In *Proceedings of the IEEE/CVF Conference on Computer Vision and Pattern Recognition*, 1768–1777.
- Zhou, L.; Du, Y.; and Wu, J. 2021. 3d shape generation and completion through point-voxel diffusion. *arXiv preprint arXiv:2104.03670*.
- Zhou, Y.; Liu, S.; and Ma, Y. 2021. NeRD: Neural 3D Reflection Symmetry Detector. In *Proceedings of the*

IEEE/CVF Conference on Computer Vision and Pattern Recognition, 15940–15949.